Rapid Communications

# Nonlinear excitation of the ablative Rayleigh-Taylor instability for all wave numbers

H. Zhang,[1] R. Betti,[1] V. Gopalaswamy,[1] R. Yan,[2] and H. Aluie[1,*]

[1]*Department of Mechanical Engineering and Laboratory for Laser Energetics, University of Rochester, Rochester, New York 14627, USA*

[2]*Department of Modern Mechanics, University of Science and Technology of China, Hefei 230026, China*

(Received 20 June 2017; published 16 January 2018)

Small-scale perturbations in the ablative Rayleigh-Taylor instability (ARTI) are often neglected because they are linearly stable when their wavelength is shorter than a linear cutoff. Using two-dimensional (2D) and three-dimensional (3D) numerical simulations, it is shown that linearly stable modes of any wavelength can be destabilized. This instability regime requires finite amplitude initial perturbations and linearly stable ARTI modes to be more easily destabilized in 3D than in 2D. It is shown that for conditions found in laser fusion targets, short wavelength ARTI modes are more efficient at driving mixing of ablated material throughout the target since the nonlinear bubble density increases with the wave number and small-scale bubbles carry a larger mass flux of mixed material.

DOI: 10.1103/PhysRevE.97.011203

Rayleigh-Taylor Instability (RTI) [1,2] occurs in a multitude of natural and engineered systems in which buoyancy forces exist. It occurs when a heavy fluid is accelerated against a light fluid and is manifested by the formation of upward-rising bubbles of the light fluid and downward-sinking spikes of the heavy fluid. Examples include the oceanic meridional overturning circulation [3], buoyant magnetic flux tubes in the solar corona [4], current sheet reconnection [5], and jet-driven lobes in the intergalactic cluster medium [6]. RTI also plays a central role in the evolution of supernova (SN) explosions [7].

RTI is a major obstacle to achieving ignition via inertial confinement fusion (ICF), which has motivated a large simulation effort [8]. In an ICF implosion, a dense spherical shell is ablated either by intense UV laser beams or soft x rays, causing an inward acceleration. Mass ablation drives a dynamic pressure as in a rocket, causing the ablated light fluid at the outer surface of the shell to push against the denser shell (or heavy fluid) during the acceleration phase, leading to the ablative RTI (or ARTI).

ARTI can dramatically degrade the capsule implosion by reducing the final compression, mixing the ablator material into the fuel, and even completely breaking up the imploding shell. The degradation of the capsule's performance depends on the extent and speed with which bubbles penetrate the heavy fluid. Understanding the nonlinear behavior of ARTI modes [9] and characterizing their excitation conditions is, therefore, essential to estimating their effect on the target performance and to ultimately determining the conditions required for achieving thermonuclear ignition.

Classical RTI theory [1] shows that a single-mode perturbation grows exponentially in the linear phase, at a rate $\gamma = \sqrt{A_T k g}$ that increases with wave number $k$, acceleration $g$, and Atwood number $A_T = (\rho_h - \rho_l)/(\rho_h + \rho_l)$. Here, $\rho_h$ and $\rho_l$ are the density of the heavy and light fluids, respectively. RTI enters the nonlinear phase when the mode amplitude exceeds a fraction of its wavelength $\lambda$, around $0.1\lambda$. In the deep nonlinear phase, the bubble reaches a terminal constant velocity as it penetrates into the heavy fluid [10,11]. The bubble velocity is $U_b^{cl} = \sqrt{g(1-r_d)/C_g k}$ with $C_g = 3$ in two dimensions (2D) and $C_g = 1$ in three dimensions (3D). Here, $r_d = \rho_l/\rho_h$ is the fluid density ratio.

It has long been argued that the ablation process produces a restoring force (dynamic pressure) and reduces the linear growth rate with respect to the classical value, especially for sufficiently short wavelength modes at which the instability is suppressed [12–17]. For large Froude numbers ($F_r = V_a^2/gL_0$), the ARTI linear growth rate can be written as $\gamma = \sqrt{A_T k g - A_T^2 k^2 V_a^2/r_d} - (1 + A_T) k V_a$ [17]. Here $V_a$ is the ablation velocity and $L_0$ is the thickness of the ablation front. In the linear regime, both theory and simulations show that mass ablation leads to a linear cutoff wave number $k_c^l$ in the unstable spectrum, beyond which the ARTI modes are linearly stable [14–17]. This has justified the common practice of neglecting short wavelength modes in ICF modeling. However, recent direct-drive studies indicate that tiny micron-size defects covering the target surface are the main cause of degradation in OMEGA high performance implosions [18–20]. Such short wavelength perturbations were previously thought to be fully stabilized by ablation. This Rapid Communication shows that all short wavelength perturbations that are linearly suppressed by ablation can be nonlinearly destabilized by finite initial perturbations above a critical amplitude. We also show that those short wavelength perturbations can efficiently mix large amounts of ablator material with the thermonuclear fuel.

The nonlinear theory [21] based on a sharp boundary approximation and the ordering of an ablative potential flow much greater than the rotational flow suggested that the ARTI beyond the linear cutoff can be excited by a finite amplitude perturbation. It was speculated that only high wave number modes with terminal bubble velocity smaller than the ablation velocity are absolutely stable for any initial amplitude. The

*hussein@rochester.edu

 

same theory also suggested that the ARTI terminal bubble velocity is unaffected by ablation and is the same as the classical value. Therefore, the critical "nonlinear cutoff" $k_c^{nl}$ can be obtained by comparing the classical terminal bubble velocity with the ablation velocity, i.e., $\sqrt{g(1-r_d)/C_g k_c^{nl}} = V_a$. However, since the small rotational flow ordering breaks down for fully developed small-scale bubbles, recent studies [22,23] have shown that the bubble velocity can be further accelerated above the classical value due to the ablation generated vorticity, which is not taken into account in the derivation of the nonlinear cutoff. In this Rapid Communication we show that all modes beyond the linear cutoff and even beyond the nonlinear cutoff can be destabilized by a finite amplitude perturbation greater than a critical value. In laser fusion targets, the finite amplitude perturbation can be induced by defects on the target surface from target fabrication [18] and laser imprinting [24]. Furthermore, we show that the perturbation amplitude required for destabilizing a mode is significantly smaller and the mode grows much faster in 3D than in 2D for the same wave number. We speculate that these results can be generalized to all instabilities that exhibit a cutoff wave number in the linearly unstable spectrum.

By defining the normalized vorticity $\omega_0 = \eta k V_a / r_d$ ($\eta$ represents the vorticity intensity), the nonlinear terminal bubble velocity can be written as $U_b^{rot} = \sqrt{g(1-r_d)/C_g k + \eta^2 V_a^2/4r_d}$. The enhancement of the terminal bubble velocity by vorticity can alter the finite amplitude excitation of the ARTI mode around the nonlinear cutoff $k_c^{nl}$. Since $r_d < 1$, the nonlinear terminal bubble velocity can always be larger than the ablation velocity when $\eta > 2$. Therefore all ARTI modes beyond the linear cutoff can be destabilized if initial perturbations are large enough to produce significant vorticity inside the bubble. Another important finding in this Rapid Communication is that these small-scale bubbles are capable of carrying large amounts of mass since the bubble density increases with the wave number, thereby making them particularly efficient at mixing materials. In this work, the excitation of the single-mode ARTI by a finite amplitude perturbation is studied numerically in the typical parameter range of direct-drive laser fusion. The simulations are carried out using the hydrodynamic code ART.

Extended to 3D in Ref. [23], ART [22] solves the single-fluid equation in Cartesian coordinates with Spitzer-Harm thermal conduction [25] and an ideal gas equation of state. In our studies, both two-dimensional (2D) and three-dimensional (3D) planar targets are investigated (Fig. 1). The initial condition of the target satisfies a quasiequilibrium state which corresponds to a typical acceleration phase of the direct-drive target designed for the National Ignition Facility (NIF) [26]. The planar approximation is valid during most of the acceleration phase as long as the target thickness, mode wavelength, and conduction zone region are much smaller than the target radius. As shown in Fig. 1(a), the target is ablated from the $Z = 0$ side with an ablation velocity $V_a = 3.5\,\mu$m/ns. The initial ablation front is located at $Z_0 = 60\,\mu$m and the maximum density is $\rho_a = 5.3\,\mathrm{g/cm^2}$. The ablated plasma at $Z < 60\,\mu$m has a higher temperature and lower density, while the unablated plasma at $Z > 60\,\mu$m is cold and dense. The characteristic thickness of the ablation front is $L_0 \approx 0.011\,\mu$m

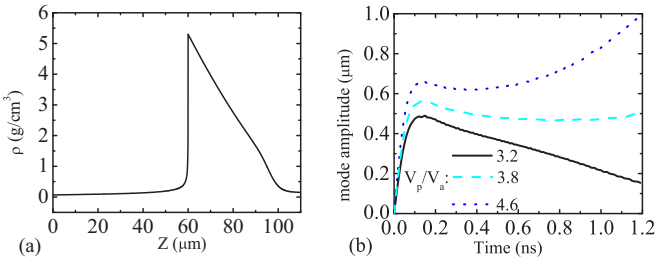


FIG. 1. (a) Initial equilibrium density profile in the $Z$ direction. (b) The time evolution of a linearly stable ARTI mode under different perturbation amplitudes, showing that it becomes unstable if the amplitude exceeds a critical value.

with the minimum density gradient scale length $L_m \approx 8.1 L_0 \approx 0.1\,\mu$m. The target material is ablated with a constant heat flux $q = 5.9\,\mathrm{MW}/\mu\mathrm{m}^2$, which is determined from the equilibrium conditions. The peak pressure of the ablated target is located at the ablation front with a value of $P_a = 120\,$Mbar. An effective gravity with an initial value of $g_0 = 100\,\mu\mathrm{m/ns}^2$ is used and adjusted in time to balance the ablative pressure such that the simulation is in a frame comoving with the ablation front. Based on the equilibrium parameters of the target, the Froude number is $F_r \approx 11$. Using Eqs. (5) and (6) in Ref. [17], it is found that the linear cutoff wave number is $k_c^l \approx 1\,\mu\mathrm{m}^{-1}$ (corresponds to a wavelength of about 6 $\mu$m). Comparing the classical terminal bubble velocity to the ablation velocity [21], as described above, yields a critical nonlinear cutoff wave number of $k_c^{nl2D} \approx 2.1\,\mu\mathrm{m}^{-1}$ and $k_c^{nl3D} \approx 5.3\,\mu\mathrm{m}^{-1}$ in 2D and 3D ARTI, respectively. It was speculated that all modes with $k > k_c^{nl}$ are stable regardless of their initial amplitude [21]. Instead, as shown here, this nonlinear cutoff is not a true cutoff in the unstable spectrum since a nonlinear finite amplitude instability exists beyond this critical wave number. In this Rapid Communication, all wave numbers are normalized with the linear cutoff wave number.

In order to excite ARTI beyond $k_c^l$, a finite amplitude velocity perturbation is initialized around the ablation front. The perturbation in the $Z$ direction has a form of $V_{pz} = V_{p0}\cos(kx)\exp(-k|z-z_0|)$in 2D simulations and $V_{pz} = 0.5V_{p0}[\cos(kx)+\cos(ky)]\exp(-k|z-z_0|)$ in 3D simulations. Meanwhile, the perturbation in the $x$ and $y$ directions has a form of $V_{ps} = V_{p0}\sin(ks)\exp(-k|z-z_0|)$ ($s = x, y$). In this case, the velocity perturbation forms a finite vortex around the ablation front. It should be noted that we have also used surface perturbations to excite the linearly stable ARTI modes, with results similar to those obtained with velocity perturbations. However, since surface density perturbations require higher grid resolution when the perturbation is small, we have mostly used initial velocity perturbations. Using very small perturbation amplitudes, we have first verified that the single-mode ARTI is linearly unstable at $k < k_c^l$ and linearly stable when $k > k_c^l$. Then, using finite perturbation amplitudes we show that a critical threshold value exists for the linearly stable ARTI modes to become nonlinearly destabilized. Figure 1(b) shows the time evolution of a typical ARTI mode beyond the linear cutoff for different initial amplitudes. The dotted blue curve represents the unstable growth triggered by

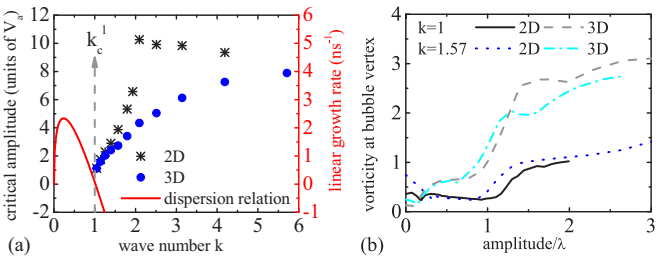


FIG. 2. (a) Critical velocity perturbation amplitude versus wave number in 2D and 3D ARTI. The linear dispersion relation (red line) is indicated by the solid red line and $Y$ axis on the right. Linear wave number cutoff is $k_c^l = 1$, while the nonlinear cutoff wave number is $k_c^{nl2D} = 2.1$ in 2D and $k_c^{nl3D} = 5.3$ in 3D. (b) Vorticity at the bubble vertex for different ARTI modes.

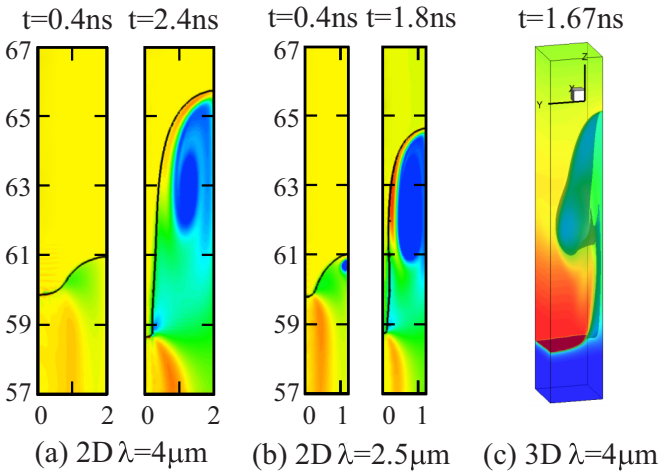


FIG. 3. Comparison of the 2D vortex structures between ARTI modes (a) $\lambda = 4\,\mu$m ($k = 1.57$) and (b) $\lambda = 2.5\,\mu$m ($k = 2.5$) at different times. Initial perturbation amplitude is $V_p = 3.6V_a$ for $\lambda = 4\,\mu$m, and $V_p = 9.9V_a$ for $\lambda = 2.5\,\mu$m. The black line shows the ablation front interface. Panel (c) is the 3D isosurface of the density for $\lambda = 4\,\mu$m.

the finite amplitude instability, while the dashed light blue curve shows the evolution in proximity of the critical unstable amplitude. The mode shown in Fig. 1(b) has wave number $k = 1.57$, which lies between the linear and the nonlinear cutoffs.

The wave number dependence of the critical amplitude required for nonlinear destabilization is shown in Fig. 2(a), for both 2D and 3D ARTI. It also shows that the 2D and 3D ARTI can be destabilized by a finite amplitude perturbation even when the wave number is beyond the nonlinear cutoff $k_c^{nl}$. The new unstable region indicates that vorticity is a primary driver of the nonlinear excitation of ARTI at $k > k_c^{nl}$, since it is the vorticity accumulation in the bubble that modifies the terminal bubble velocity. In 2D ARTI, the critical perturbation amplitude increases with wave number when $k_c^l < k < k_c^{nl2D}$, reaching a peak as $k$ approaches $k_c^{nl2D}$. Figure 2(a) shows a clear transition into a new instability regime beyond the nonlinear cutoff $k_c^{nl2D}$ where the critical amplitude slightly decreases with wave number. This result indicates that the vorticity effect becomes dominant in the ARTI destabilization at $k > k_c^{nl2D}$. Figure 2(a) also shows that the critical amplitude for the destabilization of the 3D ARTI is lower than in 2D and it converges to the 2D result when the wave number approaches the linear cutoff. Therefore, 3D ARTI is more easily destabilized than in 2D. The reduction of the critical amplitude in 3D is caused by the enhanced vorticity in 3D versus 2D for the same mode amplitude [Fig. 2(b)].

The initial perturbations required for destabilization in Fig. 2(a) can occur in ICF implosions due to isolated defects. In 2D, the largest critical velocity perturbation required for destabilization of ARTI is about $V_p \approx 10V_a$ (where the coefficient is about the size of the Froude number) and it occurs at the nonlinear cutoff wave number. This can be translated into a critical surface perturbation amplitude of about 1.4 $\mu$m if the initial perturbation is a displacement of the surface. Moreover, in a direct-drive target implosion, the ablation velocity is usually a few percent of the postshock velocity. The velocity perturbation is usually induced by variations in the postshock velocity due to nonuniform laser irradiation. Since the postshock velocity is proportional to $I^{1/3}$ ($I$ is the laser intensity on the target) [27], speckles in the laser beams with significant variations in laser intensity can imprint velocity perturbations several times larger than $V_a$.

To further investigate the role of vorticity in the destabilization of ARTI beyond the nonlinear cutoff, the unstable 2D ARTI mode structure is compared between $k = 1.57$ ($< k_c^{nl2D}$) and $k = 2.5$ ($> k_c^{nl2D}$) [Figs. 3(a) and 3(b)]. At $t = 0.4$ ns, the ARTI is mainly driven by the initial perturbation. At that time, in the $k = 1.57$ case, the instability is at the onset of the nonlinear stage and the vortex is located midway between the bubble vertex and spike tip. In the $k = 2.5$ case, the instability is in the fully nonlinear stage and a strong vortex is generated near the bubble vertex at $t = 0.4$ ns. The average vorticity within a region of size $1/k$ down from the bubble vertex is about $\omega_0 = 0.4kV_a/r_d$ and $\omega_0 = 0.94kV_a/r_d$ for the $k = 1.57$ and $k = 2.5$ simulations, respectively. The classical RTI predicts a terminal bubble velocity smaller than the ablation velocity for the $k = 2.5$ mode, in which case the ablation front overtakes the bubble and suppresses the instability. However, by exerting a centrifugal force on the bubble tip [22,23], the intense vorticity in the $k = 2.5$ mode accelerates the bubble above the classical terminal velocity and, more importantly, above the ablation velocity. It is also found that the bubble velocity is always larger than the ablation velocity for all the destabilized ARTI modes at $k > k_c^{nl2D}$. Therefore, the destabilization of the ARTI modes beyond the nonlinear cutoff is due to the enhancement of the bubble velocity by the significant vorticity produced by the initial perturbation. In contrast, the bubble in the $k = 1.57$ mode is less affected by vorticity at early times ($t = 0.4$ ns). The initial bubble velocity is below the classical value but above the ablation velocity. Therefore, it is able to grow without the aid of vorticity. In the late nonlinear phase, when the bubble is fully developed, vorticity increases and extends throughout the bubble for both $k = 1.57$ and $k = 2.5$. At this late stage, the vorticity is dominating the bubble velocity in both cases. Similar results are found in the 3D ARTI simulations. Furthermore, it is shown that the mode structure of the 3D ARTI is quite different from that of 2D ARTI (Fig. 3) in the deep nonlinear phase. In the early nonlinear

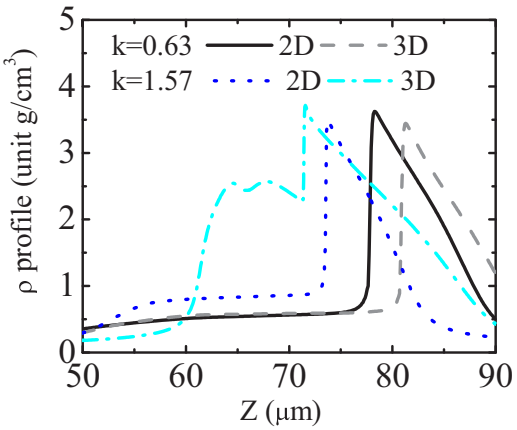


FIG. 4. The bubble density profile for 2D and 3D ARTI modes along $Z$ in the deeply nonlinear stage.

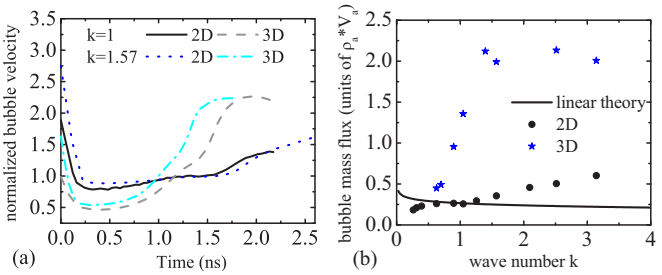


FIG. 5. (a) Time evolution of the bubble velocity normalized to the classical value. (b) Bubble mass flux for different wave numbers.

phase, the 3D spike and bubble have almost equal width. In the deep nonlinear phase, the 3D spike becomes much wider and the bubble's "stem" near the spike tip is significantly thinner [Fig. 3(c)].

As the bubble penetrates into the heavy fluid in the deeply nonlinear phase, the ablated material from the spike tip fills the inside of the bubble and is carried to the rear surface of the imploding shell. The penetration of the bubble into the target results in material mixing between the ablator on the outermost shell and the fuel during the capsule implosion, which significantly degrades the capsule performance. The denser the material inside the bubble, the greater the mixing of ablator material into the fuel. It is found that the light fluid inside the 2D bubble develops a density plateau in the nonlinear phase (Fig. 4). The density of the 2D bubble increases with wave number and is almost constant in time. In the 3D ARTI case, the bubble density is similar to the 2D results at $k < k_c^l$. However, for wave numbers beyond the linear cutoff, the density of the 3D bubbles increases with time and saturates at much higher levels than in the 2D case. The saturated density of the 3D bubbles also increases with the wave number. This result implies that 3D bubbles beyond the linear cutoff carry greater amounts of ablated material toward the opposite shell surface and are effective vehicles for driving ablator-fuel mix.

To determine the flux of light fluid material mixing into the heavy fluid, we compute the nonlinear bubble velocity for modes beyond the linear and nonlinear cutoffs. Similar to Ref. [23], we find that in the deep nonlinear phase, the bubble velocity can be significantly accelerated by the finite vorticity. Figure 5(a) shows the evolution of the bubble velocity at $k > k_c^l$. Note that the terminal bubble velocity exceeds the classical value in the deep nonlinear phase for both 2D and 3D ARTI. Since the vorticity near the 3D bubble tip is much higher than in 2D [Fig. 2(b)], the normalized terminal bubble velocity of the 3D ARTI saturates at a much higher level than the 2D ARTI for the same wave number. Considering the $\sqrt{3}$ times larger classical terminal bubble velocity, the 3D bubble penetrates into the target much faster than in 2D. In order to assess the material mixing due to ARTI, the mass flux carried by the bubble is further estimated by multiplying the terminal bubble velocity with the density of the bubble plateau [Fig. 5(b)]. It is shown that the mass flux increases with wave number and that the mass flux of the 3D bubbles is much larger than in 2D, especially when the wave number is larger than the linear cutoff. As discussed in Fig. 4, 3D bubbles beyond the linear cutoff exhibit both higher density and higher terminal velocity than in 2D, thereby enhancing their ability to drive mixing.

In summary, it is shown that small-scale ARTI modes can be excited at all wave numbers beyond the linear and the nonlinear cutoff starting from finite amplitudes above a critical value. The finite amplitude excitation is investigated in both 2D and 3D. The destabilization of the ARTI beyond $k_c^{nl}$ is due to an enhancement of the bubble velocity above the ablation velocity by strong vorticity generated by large initial perturbations. The 3D ARTI is more easily destabilized and can grow much faster than in 2D due to larger vorticity. Furthermore, a nonlinearly unstable 3D bubble saturates at a much higher bubble velocity and bubble density than in 2D. This implies that short wavelength modes in 3D ARTI are very effective at driving mix in ICF implosions and their role in setting the implosion performance should not be overlooked.

This work was supported by the DOE Office of Fusion Energy Sciences Grant No. DE-SC0014318 and the DOE National Nuclear Security Administration under Award No. DE-NA0001944. H.A. was also supported by NSF Grant No. OCE-1259794 and by the LANL LDRD program through Project No. 20150568ER. R.Y. was supported by NSFC Grants No. 11642020 and No. 11621202, and Science Challenge Project Grant No. TZ2016001. An award of computer time was provided by the INCITE program, using resources of the Argonne Leadership Computing Facility, which is a DOE Office of Science User Facility supported under Contract No. DE-AC02-06CH11357.

[1] G. I. Taylor, Proc. R. Soc. London, Ser. A **201**, 192 (1950).

[2] Lord Rayleigh, *Scientific Papers* (Cambridge University Press, Cambridge, UK, 1900), Vol. II, p. 200.

[3] C. Wunsch and R. Ferrari, Annu. Rev. Fluid Mech. **36**, 281 (2004).

[4] A. Dedner, D. Kröner, C. Rohde, and M. Wensenberg, Int. Ser. Numer. Math. **140**, 277 (2001).

[5] L. J. Guo, Y. M. Huang, A. Bhattacharjee, and D. E. Innees, Astrophys. J. Lett. **796**, L29 (2014).
[6] E. L. Blanton, T. E. Clarke, C. L. Sarazin, S. W. Randall, and B. R. McNamara, Proc. Natl. Acad. Sci. USA **107**, 7174 (2010).
[7] V. N. Gamezo, A. M. Khokhlov, E. S. Oran, A. Y. Chtchelkanova, and R. O. Rosenberg, Science **299**, 77 (2003).
[8] J. D. Lindl, *Inertial Confinement Fusion* (Springer, New York, 1998).
[9] D. Shvarts, U. Alon, D. Ofer, R. L. McCrory, and C. P. Verdon, Phys. Plasmas **2**, 2465 (1995).
[10] D. Layzer, Astrophys. J. **122**, 1 (1955).
[11] V. N. Goncharov, Phys. Rev. Lett. **88**, 134502 (2002).
[12] S. Bodner, Phys. Rev. Lett. **33**, 761 (1974).
[13] H. Takabe, K. Mima, L. Montierth, and R. L. Morse, Phys. Fluids **28**, 3676 (1985).
[14] J. Sanz, Phys. Rev. Lett. **73**, 2700 (1994).
[15] R. Betti, V. N. Goncharov, R. L. McCrory, and C. P. Verdon, Phys. Plasmas **2**, 3844 (1995).
[16] V. N. Goncharov, R. Betti, R. L. McCrory, and C. P. Verden, Phys. Plasmas **3**, 4665 (1996).
[17] R. Betti, V. N. Goncharov, R. L. McCrory, and C. P. Verdon, Phys. Plasmas **5**, 1446 (1998).
[18] I. V. Igumenschev, V. N. Goncharov, W. T. Shmayda, D. R. Harding, T. C. Sangster, and D. D. Meyerhofer, Phys. Plasmas **20**, 082703 (2013).
[19] T. C. Sangster, V. N. Goncharov, R. Betti, P. B. Radha, T. R. Boehly, D. T. Casey, T. J. B. Collins, R. S. Craxton, J. A. Delettrez, D. H. Edgell *et al.*, Phys. Plasmas **20**, 056317 (2013).
[20] V. N. Goncharov, T. C. Sangster, R. Betti, T. R. Boehly, M. J. Bonino, T. J. B. Collins, R. S. Craxton, J. A. Delettrez, D. H. Edgell, R. Epstein *et al.*, Phys. Plasmas **21**, 056315 (2014).
[21] J. Sanz, R. Betti, R. Ramis, and J. Ramírez, Plasma Phys. Controlled Fusion **46**, B367 (2004).
[22] R. Betti and J. Sanz, Phys. Rev. Lett. **97**, 205002 (2006).
[23] R. Yan, R. Betti, J. Sanz, H. Aluie, B. Liu, and A. Frank, Phys. Plasmas **23**, 022701 (2016).
[24] J. H. Gardner and S. E. Bodner, Phys. Rev. Lett. **47**, 1137 (1981).
[25] L. Spitzer and R. Harm, Phys. Rev. **89**, 977 (1953).
[26] P. W. McKenty, V. N. Goncharov, R. P. J. Town, S. Skupsky, R. Betti, and R. L. McCrory, Phys. Plasmas **8**, 2315 (2001).
[27] W. M. Manheimer, D. G. Colombant, and J. H. Gardner, Phys. Fluids **25**, 1644 (1982).